Determination of effective magnetization and gyromagnetic ratio of yttrium iron garnet from multi-mode ferromagnetic resonance S_{21} spectra

Kevin J Coakley, Pavel Kabos and Scooter D Johnson

Abstract—We acquire ferromagnetic resonance spectra for an out-of-plane magnetized yttrium iron garnet sample with a vector network analyzer at microwave frequencies ranging from 4.2 GHz to 5.2 GHz. The applied static magnetic field varies from approximately 253.6 kA/m to 260.1 kA/m. Based on an empirical model for resonant features in the S_{21} spectrum produced by the excitation of multiple modes and instrumental effects, we predict measured values of S_{21} parameters. For each of many microwave frequencies, for each of multiple modes, we determine the resonant field value of the applied magnetic field, an amplitude and a ferromagnetic resonance line width. Based on the frequency-dependent resonant field values produced by excitation of the main mode, we determine the effective magnetization and the gyromagnetic ratio of the sample.

Index Terms—Effective magnetization, ferromagnetic resonance spectra, empirical modeling, statistical methods.

I. INTRODUCTION

ONE of the recent and widely used standard techniques in broadband characterization of magnetic materials by ferromagnetic resonance (FMR) is to position the investigated material over a strip line or coplanar waveguide (CPW). Because the technique is non-resonant, it enables measurement of magnetic excitations in the investigated specimen over a broad frequency range. For a comparison of the most common techniques, see [1], [2]. Here we will focus on vector network analyzer (VNA) measurements. The advantage of the VNA approach is its full amplitude and phase characterization capabilities. The FMR parameters are obtained from standard scattering S parameters as a function of the frequency and applied magnetic field where the field is fixed and the frequency varied (swept) as in [1], [2], or the frequency is fixed and the applied magnetic field is swept (for an example, see [3]). A typical measurement setup utilizes a CPW that operates over a broad frequency range– typically 1 GHz to 40 GHz. A sample is mounted in a "flip-chip" setup in close proximity to the conductor line so that the material undergoes FMR at the selected field and frequency. The resulting absorption is detected by the VNA. For analysis of a single resonance mode based on frequency-swept VNA-FMR measurements, see [1], [2]. The procedure for subtracting background from field

Kevin J Coakley is with the National Institute of Standards and Technology, Boulder, CO, 80305 USA (email: kevin.coakley@nist.gov)

Pavel Kabos is with the National Institute of Standards and Technology, Boulder, CO, 80305 USA

Scooter D Johnson is with the US Naval Research Laboratory, Washington, DC 20375 USA

swept VNA-FMR measurement is presented in [4]. The above mentioned examples are for the case where the analyzed FMR spectrum corresponds to a single uniform mode excitation. For this case, the field sweep can be designed so that the measured spectra corresponds to either a uniform precession mode for a sample with a large linewidth mode, or for a large area sample. Usually, only the uniform precession mode is observed. In contrast, very low-loss materials like yttrium iron garnet (YIG) may yield a more complicated FMR signal. For instance, broad frequency or field sweeps, particularly in dimensionally restricted samples such as thin film magnetostatic mode YIG waveguides [5], [6], [7], patterned YIG [8], 2D magnonic crystals [9], patterned multilayer structures [10], and magnetic nanowires [11], excite a large number of modes and produce multi-mode FMR spectra. The degree of separation of features in such multi-mode FMR spectra depends on the film dimensions. For example, as the thickness of a low-loss film increases but all other dimensions remain fixed, the separation between resonant values of the applied field decrease. The applications of YIG films and spheres are well-established and growing. Potential new applications areas including spin-based electronics and quantum computing. Unfortunately, in contrast to the well-established characterization of measured single-mode excitation spectra discussed in the above references, there is almost no effort to characterize magnetic material properties based on multi-mode FMR spectra. This study utilizes the VNA techniques in a field-swept configuration with the sample surface normal vector oriented parallel to the applied field, referred herein as the out-of-plane (OOP) orientation. Measurements in this study were taken with a CPW with metal backing. The signal line was 50 μm wide with no spacer between the waveguide and the sample. To provide an adequate ground connection, the top-side ground plane was electrically connected to the backside ground plane with an array of vias that extended along the path of the conductor. This configuration ensured a good response up to 40 GHz. The VNA was calibrated by a standard short-open-load-through method [12] out to the end of the coaxial cables. The VNA power was fixed at 0 dBm. At each fixed frequency, measurements were acquired as a function of the bias magnetic field with LabVIEW [13] software. Here, we develop a method to determine relevant magnetic material parameters from multi-mode experimental spectra. As an illustration, we apply our method to VNA-FMR field-swept measurements on an magnetized OOP 5 μm thick single-crystal YIG 5 mm x 5 mm square film grown on a $Gd_3Ga_5O_{12}$

(GGG) substrate by liquid phase epitaxy (LPE). The film was manufactured by [14]. We note that in a low-loss YIG film, experimental data indicates that a mixture of magnetostatic modes and standing wave modes are excited at various depths. The proposed procedure is universal and can be also applied to frequency-swept VNA-FMR measurements of OOP magnetic materials.

II. METHODS

A. Physical Model for Magnetic Susceptibility

The magnetization dynamics is described by the Landau-Lifshitz equation (LLE) with a damping term. For an OOP magnetized film with OOP uniaxial anisotropy, the magnetic susceptibility as derived from LLE can be expressed as [3], [15],

$$\chi(H) = \frac{M_{eff}(H - M_{eff})}{((H - M_{eff})^2 - (\frac{2\pi f}{\gamma \mu_o})^2) - i(\Delta H(H - M_{eff}))}, \quad (1)$$

where $M_{eff} = M_s - H_k^{\perp}$, $\mu_o = 4\pi \times 10^{-7}$ N/A^2 is the vacuum magnetic permeability, M_s is the saturation magnetization, $H_k^{\perp}$, is the out-of-plane anisotropy field, ΔH is the linewidth, H is the applied magnetic field, f is frequency, $\gamma = g\mu_B/\hbar =$ 1.760 859 770$\times 10^{11}$ s^{-1}T^{-1} is the gyromagnetic ratio of the free electron, g is the Lande´ spectroscopic splitting factor, μ_B is the Bohr magneton, and $\hbar$ is the reduced Planck constant. In this work, we express all quantities in SI units. In our analysis of the S_{21} spectrum due to multi-mode excitations, we make the ad hoc assumption that each of the resonant features can be modeled similar to how the susceptibility of the uniform precession mode is modeled by Eq. 1. Each resonant feature is characterized by an amplitude, resonant field and linewidth. According to Kittel's equation for an OOP magnetized film, the resonant field value for the main mode, H_{r*} varies with frequency as

$$H_{r*} = M_{eff} + \frac{2\pi f}{\gamma \mu_o}. \quad (2)$$

Rewriting Eq. 2 and assuming that $M_{eff} = M_s$,

$$M_s = H_{r*} - \frac{2\pi f}{\gamma \mu_o} \quad (3)$$

B. Empirical prediction model for S_{21}

Here, we measure S_{21} scattering parameters with a VNA with methods similar to those described in [1] and [2]. We model the contribution of each excited mode to the theoretical S_{21} spectrum with a generalization of Eq. 1. For each excited mode, we define an empirical prediction term S as

$$S(H) = \tilde{A}(H - H_r + \frac{2\pi f}{\gamma \mu_o})\ ]\ /$$

$$[\ (H - H_r + \frac{2\pi f}{\gamma \mu_o})^2 - (\frac{2\pi f}{\gamma \mu_o})^2\ +$$

$$i\kappa(\Delta H(H - H_r + \frac{2\pi f}{\gamma \mu_o})\ ], \quad (4)$$

where H_r and $\tilde{A}$ are the resonant field value and amplitude of the feature generated by a mode, and κ is equal to either -1 or 1 (for all modes).

The real and imaginary parts of S are

$$\text{Re}(S(H)) = \frac{\tilde{A}}{D}(H - H_r + \frac{2\pi f}{\gamma \mu_o}\ )\times$$

$$(\ (H - H_r + \frac{2\pi f}{\gamma \mu_o})^2 - (\frac{2\pi f}{\gamma \mu_o})^2\ ), \quad (5)$$

and

$$\text{Im}(S(H)) = -\frac{\tilde{A}\kappa}{D}\Delta H(H - H_r + \frac{2\pi f}{\gamma \mu_o})^2, \quad (6)$$

where

$$D = (\ (H - H_r + \frac{2\pi f}{\gamma \mu_o})^2\ -\ (\frac{2\pi f}{\gamma \mu_o})^2\ )^2\ +$$

$$(\ \Delta H(\ H - H_r + \frac{2\pi f}{\gamma \mu_o}\ )\ )^2. \quad (7)$$

At $H = H_r$, $\text{Re}(S) = 0$ and $\text{Im}(S)$ takes its maximum or minimum value depending on the signs of κ and $\tilde{A}$. For a model with K modes, the overall value of S is

$$S(H) = \sum_{k=1}^{K} S_k(H), \quad (8)$$

where S_k is the theoretical contribution due to the kth mode. The contribution of each distinct mode to S depends on three model parameters: $\tilde{A}$, H_r and ΔH which, in general, vary from mode-to-mode.

Given S, we model the theoretical value of S_{21} as

$$S_{21}(H) = B(H) + \exp(i\phi)S(H), \quad (9)$$

where the phase parameter falls in the interval $[0, 2\pi]$, and the theoretical background, $B(H)$, is a linear function of H. That is,

$$B(H) = \alpha + \beta H, \quad (10)$$

where α and β are complex constants to be determined. Given that $(\text{Re}(\alpha), \text{Im}(\alpha)) = (\alpha_r, \alpha_i)$ and $(\text{Re}(\beta), \text{Im}(\beta)) = (\beta_r, \beta_i)$, we have that

$$\text{Re}(S_{21}(H)) = \alpha_r + \beta_r H \quad (11)$$

$$+ \sum_{k=1}^{K} (\ \cos(\phi)\text{Re}(S_k(H)) - \sin(\phi)\text{Im}(S_k(H))\ ),$$

and

$$\text{Im}(S_{21}(H)) = \alpha_i + \beta_i H$$

$$+ \sum_{k=1}^{K} (\ \sin(\phi)\text{Re}(S_k(H)) + \cos(\phi)\text{Im}(S_k(H))\ ), \quad (12)$$

where K is the number of modes in our model.

In general, a feature in the FMR spectrum could be due to a single mode or multiple modes that closely overlap. Here, we model each feature as due to a single mode. If there are K modes in the model fit to data, we refer to such a model as a K-feature model.

C. Estimation of model parameters

For each feature, we must estimate three model parameters: $\tilde{A}$, H_r and ΔH which, in general, vary from feature-to-feature. We must also estimate a phase ϕ and four background parameters α_r, α_i, β_r, and β_i. Hence, for a model with K features, the total number of model parameters is 3K+5. We denote these parameters as a (3K+5)-dimensional vector θ. We determine θ with a two-stage stochastic optimization method. In this approach, we seek to minimize the mean-square-deviation between predicted and observed pooled spectra (from both the real and imaginary parts of S_{21}) with a modified Levenberg-Marquardt [16] method where we specify a lower and upper bound for each model parameter estimate. In stage 1, we simulate N_{sim} random realizations of θ. Each random initial parameter value is sampled from a Gaussian distribution with mean equal to the average of its lower and upper bound, and standard deviation equal to one-tenth the difference of its upper and lower bounds. For each simulated initial value of θ, we determine a final estimate (and associated value of the cost function) with the Levenberg-Marquardt method. We select the estimate that yields the lowest value of the cost function.

In stage 2, we simulate N_{sim} random initial estimates of θ like in stage 1, but with one major difference. In stage 2, the central value of the sampling distribution is the estimate determined in the first stage rather than the average of the upper and lower bounds. If a simulated value of a model parameter falls outside its allowed interval, we set it to the corresponding central value in the simulation model. Like in stage 1, we determine a final estimate and associated cost function for each of N_{sim} simulated initial values of θ with the Levenberg-Marquardt method, and select the one that yields the lowest value of the cost function. The selected value from the stage 2 analysis is the final estimate. The primary results reported here correspond to $N_{sim} = 2000$.

Each stage of our procedure is an example of a multi-start [17] method for avoiding getting stuck in a local minimum of the cost function. (see Appendix for more details).

III. RESULTS

A. Analysis for each frequency.

We analyze FMR spectra at microwave frequencies that range from 4.2 GHz to 5.2 GHz. At each frequency, the strength of the applied magnetic field H varies from approximately 253.6 kA/m to 269.1 kA/m.

In our primary study, at each frequency, we fit a six-feature model to observed spectra. Here, we constrain each amplitude ($\tilde{A}$) estimate to be non-negative, set $\kappa = 1$ in our Eq. 4 prediction model, and similar to the approach in [3], set γ to the nominal value corresponding to the gyromagnetic ratio of the free electron. We stress that when $\kappa = -1$, we obtained poor results. To illustrate our methods, we show predicted and observed S_{21} spectra and associated residuals for the 4.2 GHz frequency case in Figure 1, and list associated model parameter estimates in Table 1. In Figure 1a, we show estimates of the resonant field values for the six features as vertical dashed lines. For other frequencies, the visual agreement between observed and predicted spectra is similar
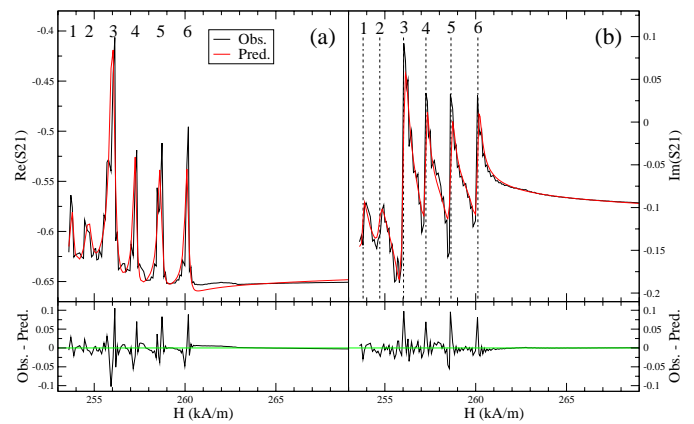

Fig. 1.   Top: Observed and predicted values of the real (a) and imaginary(b) part of S_{21} at $f = 4.2$ GHz. Dashed vertical lines show estimated locations of resonant values of the applied field for each of the six features. Bottom: We show residuals. In our analysis, we set γ to to the gyromagnetic ratio of the free electron ($1.760\,859\,770 \times 10^{11}$ $s^{-1}T^{-1}$).

TABLE I
SIX-FEATURE MODEL RESULTS FOR $f = 4.2$ GHz CASE. WE SET THE GYROMAGNETIC RATIO FOR THE SAMPLE TO THE GYROMAGNETIC RATIO OF THE FREE ELECTRON. THE ESTIMATES OF α_r AND α_i ARE -0.766 AND AND 0.048 RESPECTIVELY. THE ESTIMATES OF β_r AND β_i (IN UNITS OF METERS/KILOAMPERES) ARE 3.57×10^{-5} AND -4.51×10^{-5}. THE ESTIMATED VALUE OF ϕ IS 109.55 DEGREES.

feature	$\tilde{A}$ (A/m)	H_r (kA/m)	ΔH (kA/m)	range of predicted Re(S)
1	13.51	253.800	0.237	0.054
2	19.86	254.719	0.426	0.046
3	84.08	256.027	0.339	0.241
4	29.45	257.259	0.223	0.130
5	32.50	258.638	0.272	0.114
6	29.11	260.119	0.236	0.123

TABLE II
SIX-FEATURE MODEL RESULTS FOR MAIN MODE (THIRD) FEATURE FOR ALL f VALUES. WE SET THE GYROMAGNETIC RATIO FOR THE SAMPLE TO THE GYROMAGNETIC RATIO OF THE FREE ELECTRON

. Below, the RMS deviation is the root-mean-square deviation between predicted and observed values of the real and imaginary parts of S_{21}.

f (GHz)	$\tilde{A}$ (A/m)	H_r (kA/m)	ΔH (kA/m)	RMS
4.2	84.08	256.027	0.339	0.0178
4.3	83.38	258.954	0.310	0.0182
4.6	106.18	267.828	0.390	0.0195
4.8	104.31	273.703	0.351	0.0224
4.9	111.14	276.564	0.364	0.0219
5.0	99.87	279.545	0.327	0.0206
5.2	107.17	285.350	0.341	0.0210

to the visual agreement for the 4.2 GHz case (see Figure 2). The root-mean-square (RMS) deviation between observed and predicted spectra varied from 0.0178 to 0.0224 for the seven frequencies of interest (see Table 2).

B. Determination of M_{eff} and γ

We identify the feature produced by the main mode as the one with the largest range (maximum minus minimum) of predicted values of Re(S) (see Eq. 5) over all values of H in the analyzed FMR spectrum (Table 1 and Figures 1 and 2). For each frequency, this selection rule identifies the third feature as
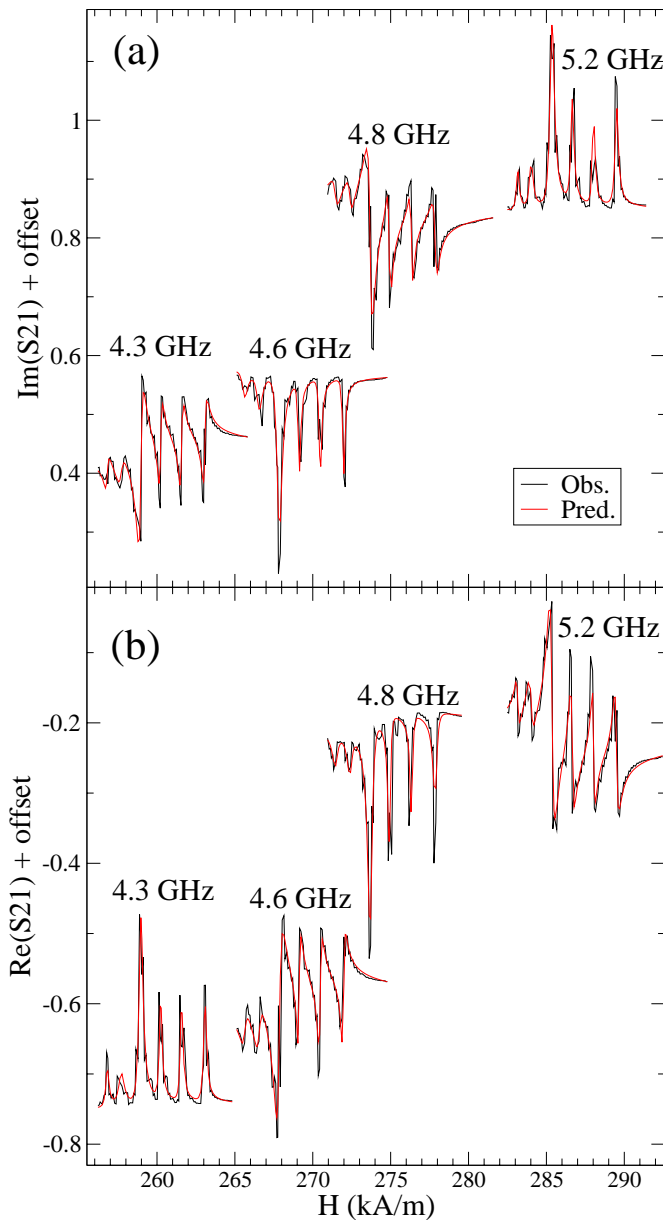
Fig. 2. Predicted (red lines) and observed (black lines) for S_{21} spectra at $f = (4.3, 4.6, 4.8$ and $5.2)$ GHz. The median values of the measured real and imaginary parts of the S_{21} spectrum at $f = (4.3, 4.6, 4.8$ and $5.2)$ GHz are (-0.600, 0.222, 0.626, -0.199) and (0.234, 0.600, 0.118, -0.605) respectively. Here, to facilitate visual inspection of results, we show spectra that are translated vertically by a frequency-dependent offset that, for any frequency, varies for the real and imaginary parts of S_{21}. The value of γ is set to same value an in Figure 1 analysis.

that produced by the main mode. For the measurements studied here, the estimated amplitude associated with the selected feature is larger than the amplitudes associated with the non-selected features (Table 1). Based on Eq. 2, we model our estimate of the resonant field value associated with the main mode at f as $\hat{H}_{r*}(f)$ where

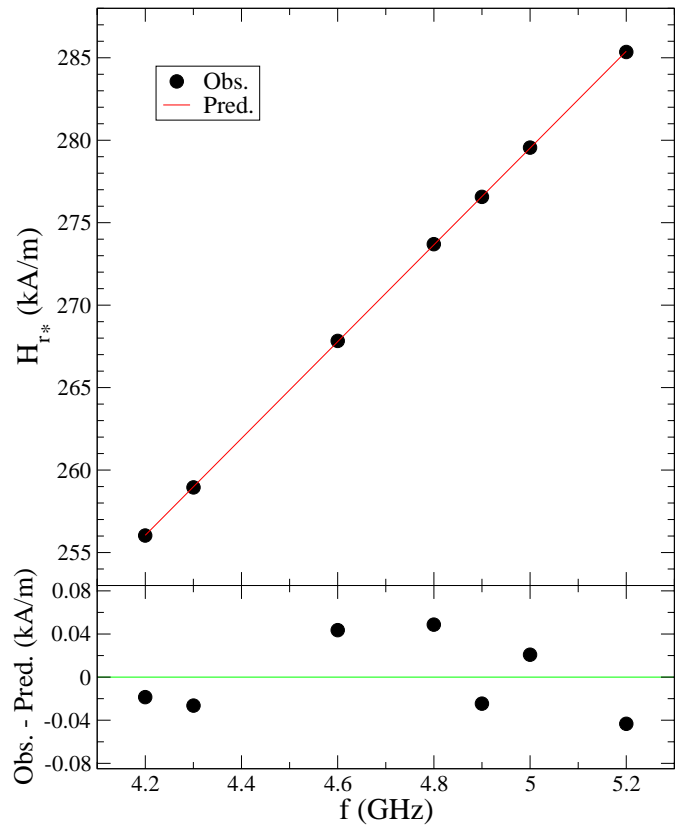$$\hat{H}_{r*}(f) = M_{eff} + \frac{2\pi f}{\gamma \mu_o} + \epsilon(f). \tag{13}$$

Fig. 3. Top: Estimated resonant field values of the main mode versus microwave frequency (see Table II) and predicted values based on fitting the Eq. 13 model to observed data by the method of ordinary least squares. Our estimates of M_{eff} and γ are 132.79(0.52) kA/m and 1.7037(0.0065)$\times 10^{11}$ s^{-1}T^{-1}. Bottom: Residuals.

Above, $\epsilon(f)$ is measurement error and M_{eff} and γ^{-1} are theoretical parameters that we determine by ordinary least squares with the **R** [19] function **lm** (see Figure 3). In this linear regression approach, γ^{-1} and M_{eff} are slope and intercept parameters. Our estimate of γ is the reciprocal of our estimate of γ^{-1}. Given the uncertainty of estimated γ^{-1} reported by the statistical software, we determine the uncertainty of estimated γ by the propagation of uncertainty method [21]. Our estimates of M_{eff} and γ are 132.79(0.21) kA/m and 1.7037(0.0026)$\times 10^{11}$ s^{-1}T^{-1} respectively. The estimates and uncertainties (in parentheses) are determined under the assumption that the model is valid and random measurement errors at different frequencies have the same variance and are uncorrelated. The statistical software reports the standard deviation of the random measurement error of H_{r*} at each frequency to be 0.041 kA/m based on standard linear regression theory [18].

We can not rule out the possibility that measured values of the resonant field for the main mode at different frequencies are affected by frequency-dependent systematic errors. We quantify additional components of uncertainty that account for this possible systematic effect on estimates of M_{eff} and γ. We split the data shown in upper frame of Figure 3 into two subsets. One corresponds to $f \leq 4.6$ GHz, the other to $f \geq 4.8$ GHz. For each subset, we determine estimates of M_{eff} and γ. For the two subsets, the magnitude of the difference in the

estimates of M_{eff} and γ are 1.66 kA/m and 2.06×10^9 T^{-1}s^{-1} respectively. For each model parameter, following [21], we quantify an additional component of uncertainty to be the standard deviation of a uniform distribution that has width equal to the magnitude of the relevant difference of estimates for the two subsets. The additional uncertainty components for M_{eff} and γ are 0.48 kA/m and 5.9×10^8 s^{-1}T^{-1}. Thus, the combined uncertainties of our estimates due to random effects and the systematic effect are 0.52 kA/m and 6.5×10^8 s^{-1}T^{-1}. As a caveat, other systematic effects may influence our estimates of M_{eff} and γ.

C. Discussion

1) Amplitude constraint: As discussed earlier, in our primary study, we constrain the amplitude estimates to be non-negative. In a secondary study, we removed this constraint and allowed amplitude estimates to be positive or non-positive. In this secondary study, at each frequency, the signs of the estimated amplitudes were the same for all six features. However, the signs varied from frequency to frequency. Nonetheless, for each frequency, the difference in the magnitude of the estimated amplitude for any particular feature determined in the two studies was negligible. Moreover, at any frequency, the difference between predicted FMR spectra was negligible. We attribute discrepancies in the signs to the fact that if the phase ϕ in our Eq. 9 model is shifted by π and the estimated amplitudes are scaled by -1, both $\exp(i\phi)$ and $S(H)$ will change sign but their product will not.

2) Choice of N_{sim}: We set γ to its nominal value and obtained results for N_{sim} = 1000, 2000, 4000 and 8000. For each frequency, the RMS deviations between observed and predicted S_{21} spectra determined for the different choices of N_{sim} agreed to within 1.2×10^{-11} percent or less. Relative to the N_{sim} = 2000 case, the difference between estimated M_{eff} determined for N_{sim} = (1000,4000,8000) are (-2.3, -5.9, -8.1)$\times10^{-6}$ kA/m. The differences between γ estimates are (-4.0,-7.3,-11.1)$\times10^3$ s^{-1}T^{-1}. Relative to reported uncertainties for M_{eff} and γ (0.52 kA/m and 6.5×10^8 s^{-1}T^{-1}), these differences are negligible.

3) Choice of γ: As a consistency check, we determined the resonant field values for the seven frequencies for the case where γ equals the empirical estimated reported in Section III B. The resulting differences in the estimated resonant field values ranged from -7.5×10^{-6} kA/m to -2.5×10^{-6} kA/m. The differences in the empirical estimates of M_{eff} and γ determined by fitting the Eq. 13 model to the updated resonant field values, relative to our primary study result, -8.1×10^{-6} kA/m and -4.1×10^3 s^{-1}T^{-1}, are negligible relative to reported uncertainties.

4) Model choice: We fit a 5-feature model to the same spectra as previously analyzed, and determined model parameters for features 2,3,4,5 and 6. The estimates of the resonant field values for the main mode for the seven frequencies increased, on average, by 0.011 kA/m. However, the differences between the estimates of M_{eff} and γ determined by the 5-feature and 6-feature models, 0.0074 kA/m and -3.4×10^6 s^{-1}T^{-1} are negligible relative to reported uncertainties.

5) Random uncertainty of measured H_{r*}: In Section III-B we determined the random uncertainty of measured H_{r*} at each frequency to be 0.041 kA/m. Based on the assumption that random measurement errors have the same standard deviation and are uncorrelated, the statistical software that implemented the Levenberg-Marquadt method reported random uncertainties for measured H_{r*} at each frequency that ranged from 0.010 kA/m to 0.012 kA/m. A possible explanation for the discrepancy between these uncertainties and the Section III-B reported uncertainty is violation of the modeling assumption that additive measurement errors have the same standard deviation. This hypothesis is supported by the residual plot in Figure 1b. Analysis of multiple (at least 20) spectra at each frequency may be required to fully understand this discrepancy. Because of this discrepancy, we do not report uncertainties for any of the estimated model parameters listed Tables I and II.

6) Application to other experimental data: We anticipate that our method will perform well for multi-mode FMR spectra with more features (say up to 20) that are as well-separated as those in this this study. How well our method works for features that are not well-separated is a subject for further study. In this study, we determined the number of features by scientific judgement. In more complicated cases where features are not as well-separated as in thus study, it may be helpful to select the number of features by statistical learning methods such as cross-validation [22], [23] In other studies, features of interest in multi-mode FMR spectra might not be as well-separated as in this study. For more complicated cases, a more complicated stochastic optimization method may be required.

IV. CONCLUSION

For a YIG sample, we determined a resonant field value, linewidth and amplitude for each of many features produced by a multi-mode excitation. Based on analysis of the main feature for microwave frequencies ranging from 4.2 GHz to 5.2 GHz, we determined the effective magnetization and gyromagnetic ratio of the YIG sample.

APPENDIX
MODEL PARAMETER ESTIMATION METHOD

For a model with K features, we estimate a (3K+5)-dimensional model parameter vector θ by minimizing the following cost function

$$C = \sum_j (\ \epsilon_{Re}^2(j) + \epsilon_{Im}^2(j)\ )$$

where $\epsilon_{Re}(j)$ is the difference between the observed and predicted value of the real part of S_{21} at $H = H_j$ (see Eq. 5), and $\epsilon_{Im}(j)$ is the difference between the observed and predicted value of imaginary part of S_{21} at $H = H_j$ (see Eq. 6).

As described in section II-C, for each of many randomly general initial values of our model parameter vector θ, we determine an approximate global minimum of C with a modified Levenberg-Marquardt [16] method where we specify a lower and upper bound for each component of θ. We implement our optimization with public domain **R** [19] software. In particular, we call the function **nls.lm**, from the package **minpack.lm** [20].

The lower and upper bounds for each linewidth parameter ΔH are 0.008 kA/m and 0.8 kA/m. The lower and upper bounds for each resonant field value H_r are centered about an initial estimate $\tilde{H}_r$ determined from a peak finding analysis of the spectra. For each feature, we set $\tilde{H}_r$ to the location of a local extremum of the imaginary part of S_{21}. For example, for the 4.2 GHz case, we set initial estimates to the locations of local maxima of the imaginary part of S_{21}. For each feature, the search interval is [$\tilde{H}_r$ - 0.8, $\tilde{H}_r$ + 0.8] kA/m. For the angle ϕ, the bounds are 0 and 2π. For α_r and α_i the bounds are -2 and 2 respectively. For β_r and β_i, the bounds are -0.0126 m/kA and 0.0126 m/kA respectively. The lower and upper bounds on estimates of $\tilde{A}$ are 0 and 8 kA/m respectively in our primary analysis.

ACKNOWLEDGMENTS

REFERENCES

[1] S. S. Kalarickal, P. Krivosik, M. Wu, C. E. Patton, M. L. Schneider, P. Kabos, T. J. Silva, and J. P. Nibarger, Ferromagnetic resonance linewidth in metallic thin films: Comparison of measurement methods, *Journal of Applied Physics* vol. 99, 093909 (2006).

[2] C. Bilzer, T. Devolder, P. Crozat, C. Chappert, S. Cardoso, and P. Freitas, Vector network analyzer ferromagnetic resonance of thin films on coplanar waveguides: Comparison of different evaluation methods, *Journal of applied physics* vol. 101, 074505 (2007).

[3] H. Nembach, T. Silva, J. M. Shaw, M. Schneider, M. Carey, S. Maat, and J. Childress, Perpendicular ferromagnetic resonance measurements of damping and Landé g- factor in sputtered (Co 2 Mn) 1- x Ge x thin films, *Physical Review B* vol. 84, 054424 (2011).

[4] A. J. Berger, E. R. Edwards, H. T. Nembach, A. D. Karenowska, M. Weiler, and T. J. Silva, Inductive detection of fieldlike and dampinglike ac inverse spin-orbit torques in ferromagnet/normal- metal bilayers, *Physical Review B* vol. 97, 094407 (2018).

[5] J. Adam, S. Talisa, and J. Kerestes, Non-destructive evaluation of yig films by ferromagnetic resonance, *IEEE Transactions on Magnetics* vol. 25, pp. 34883490 (1989).

[6] C. Sandweg, Y. Kajiwara, K. Ando, E. Saitoh, and B. Hillebrands, Enhancement of the spin pumping efficiency by spin wave mode selection, *Applied Physics Letters* vol. 97, 252504 (2010).

[7] S. Klingler, A. V. Chumak, T. Mewes, B. Khodadadi, C. Mewes, C. Dubs, O. Surzhenko, B. Hillebrands, and A. Conca, Measurements of the exchange stiffness of yig films using broadband ferromagnetic resonance techniques, *Journal of Physics D: Applied Physics* vol. 48, 015001 (2014).

[8] E. R. Edwards, M. Buchmeier, V. E. Demidov, and S. O. Demokritov, Magnetostatic spin-wave modes of an in-plane magnetized garnet-film disk, *Journal of Applied Physics* vol. 113, 103901 (2013).

[9] A. Manzin, G. Barrera, F. Celegato, M. Co sson, and P. Tiberto, Influence of lattice defects on the ferromagnetic resonance behavior of 2d magnonic crystals, *Scientific Reports* vol. 6, 22004 (2016).

[10] G. De Loubens, V. Naletov, O. Klein, J. B. Youssef, F. Boust, and N. Vukadinovic, Magnetic resonance studies of the fundamental spin-wave modes in individual submicron cu/nife/cu perpendicularly magnetized disks, *Physical Review Letters* vol. 98, 127601 (2007).

[11] Y. Zhang, J. Um, W. Zhou, B. Stadler, and R. Franklin, Magnetic nanowires for rf applications: Ferromagnetic resonance and permeability characterization, in 2019 IEEE MTT-S International Microwave Symposium (IMS) (IEEE, 2019) pp. 1100 1103.

[12] R. A. Ginley, "Establishing traceability for SOLT calibration kits," *2017 90th ARFTG Microwave Measurement Symposium (ARFTG)*, Boulder, CO, 2017, pp. 1-4, doi:10.1109/ARFTG.2017.8255871.

[13] C. Elliott, V. Vijayakumar, W. Zink, R. Hansen R. "National Instruments LabVIEW: A Programming Environment for Laboratory Automation and Measurement," JALA: Journal of the Association for Laboratory Automation. 2007;12(1):17-24 (2007). doi:10.1016/j.jala.2006.07.012.

[14] Metamagnetics, 115 Flanders Road, Suite 135, Westborough, MA 01581-1087.

[15] I. S. Maksymov and M. Kostylev, Broadband stripline ferromagnetic resonance spectroscopy of ferromagnetic films, multilayers and nanostructures, *Physica E: Low-dimensional Systems and Nanostructures* vol. 69, 253293 (2015).

[16] J. J. More, The Levenberg-Marquardt algorithm: implementation and theory, in *Numerical analysis* (Springer, 1978) pp. 105116.

[17] R. Marti, M. G. Resende, and C. C. Ribeiro, Multistart methods for combinatorial optimization, *European Journal of Operational Research* vol. 226, 18 (2013).

[18] N. R. Draper and H. Smith, Applied regression analysis. Vol. 326 (John Wiley & Sons, 1998).

[19] R Core Team, R: A Language and Environment for Statistical Computing, R Foundation for Statistical Computing, Vienna, Austria (2018). url = https://www.R-project.org/

[20] Timur V. Elzhov, Katharine M. Mullen, Andrej-Nikolai Spiess and Ben Bolker, minpack.lm: R Interface to the Levenberg-Marquardt Nonlinear Least-Squares Algorithm Found in MINPACK, Plus Support for Bounds, note = R package version 1.2-1, url = https://CRAN.R-project.org/package=minpack.lm, 2016

[21] Barry N. Taylor and Chris E. Kuyatt, "Guidelines for evaluating and expressing the uncertainty of NIST measurement results," Tech. Rep., NIST Technical Note 1297, 1994.

[22] M. Stone, Cross-validatory choice and assessment of statistical predictions, *Journal of the Royal Statistical Society: Series B (Methodological)* vol. 36, pp. 111133 (1974).

[23] S. Arlot, A. Celisse, et al., A survey of cross-validation proce- dures for model selection, *Statistics Surveys* vol, 4, 4079 (2010).